Bubble-driven liquid flows

By F. DURST,

Lehrstuhl für Strömungsmechanik, Universität Erlangen-Nürnberg, Egerlandstr. 13,
8520 Erlangen, FRG

B. SCHÖNUNG,

Institut für Hydromechanik, Universität Karlsruhe, Kaiserstr. 12, 7500 Karlsruhe 1, FRG

K. SELANGER

Norwegian Hydrodynamic Laboratories, Klaebuveien 153, 7001 Trondheim, Norway

AND M. WINTER

Institut für Hydromechanik, Universität Karlsruhe, Kaiserstr. 12, 7500 Karlsruhe 1, FRG

Detailed information is provided in this paper on the physics of momentum transfer in bubble-driven liquid flows. Experimental information is obtained on the flow around bubbles and on the axisymmetric bubble-driven liquid flow inside liquid-filled cylinders located with their axes in the vertical direction. A laser-Doppler anemometer extended for particulate two-phase flows is employed for these measurements to yield local fluid velocity information as well as the rise velocity of bubbles. The bubble top radius and the bubble shape were also found from these measurements.

Utilizing experimentally gained information and employing the basic equations for particulate *two-phase flows*, permits finite difference equations to be formulated that allow bubble-driven liquid flows to be computed. Results are presented for boundary conditions corresponding to those of the experimental studies. Comparisons of numerical and experimental results are shown to be in good agreement. This is taken as a justification to employ the developed computer programs to carry out parameter studies for bubble-driven liquid flow inside circular cylinders. Results of these studies are presented and discussed.

1. Introduction

For single-phase flows, basic knowledge of simple flows is available from analytical and/or numerical solutions of the fluid mechanics equations. These solutions are supported and/or extended by experimental results yielding basic information on momentum transport in single-phase flows. Such information is not available to the same extent for two-phase flows for the following reasons:

(i) Research work in two-phase flows is often more concerned with solutions to practical problems than the gain of basic knowledge.

(ii) Experimental investigations of two-phase flows require refined experimental techniques that have only recently become available.

(iii) Analytical and/or numerical treatments of the basic two-phase flow equations are not readily available.

These reasons apply to two-phase flows in general and to bubble-driven liquid flows in particular. Because of this, bubble-driven liquid flows are not readily understood.

No generally accepted method has been developed to analytically or numerically study such flows and provide information on the fluid flow field and on the bubble motion. The present paper tries to remedy this situation by providing a numerical solution procedure that allows the bubble-rise velocity and the fluid velocity to be numerically computed from the two-phase-flow equations of motion. Laser-Doppler measurements of the flow around rising bubbles are also given to support the numerical studies and result in information on the bubble velocity and the bubble shape. Two sets of results are provided and these measurements are shown to add to the existing knowledge of the motion of rising bubbles.

Laser-Doppler velocity measurements of the liquid flow inside a cylindrical container are also presented. This flow is driven by the rising bubbles and it is shown to consist of a rising flow in the centre part of the container and a downward flow on the outside. Experimental information is provided for various bubble frequencies and for two test cases with different bubble Reynolds and Eötvös numbers. The general differences in the shape and motion of the bubbles and the corresponding liquid motion are discussed. The bubble motion is influenced by surface impurities which reduce the 'bubble surface mobility'. This is experimentally recorded and is employed as the basis of a theoretical approach to deal with the motion of rising bubbles under the influence of bubble interface stiffening caused by impurities in the liquid.

Numerical information is obtained through solutions of the basic differential equations of particulate *two-phase flows* and for the boundary conditions corresponding to those of the experiments. The region where the bubbles rise is treated as a region of finite void with a void fraction being computed from the bubble diameter (or the bubble volume) and the bubble frequency. This information is sufficient to compute the entire flow field driven by the bubbles. The results of the experimental and numerical investigations are shown to be in good agreement.

The theoretical (numerical) investigations are extended to take into account the 'bubble stiffening' by impurities inside the interface layer. A phenomenological theory is presented which fully explains the experimental findings. The agreement between the experimental and numerically obtained results is taken as a justification for making further predictions for different parameters influencing bubble-driven liquid flows. Some results of these studies are presented in this paper together with suggestions for further research on this topic.

2. Some information on fluid particle motion

In this section, an attempt is made to provide a brief summary of the existing knowledge of various aspects of particle motion in fluids, with particular attention being given to the motion of bubbles in liquids. No attempt is made to provide a complete description of the extensive experimental and theoretical knowledge that is available in literature. For more complete information see Clift, Grace & Weber (1978), Harper (1972) or Auton (1984). The following sections are only meant as an introduction to the field and to provide some guidance to the many papers on the various aspects of particle motion in fluids.

2.1. *Similarity parameters*

To describe the dynamics of fluid particles moving within another infinitely extended fluid, if the two fluids do not mix, the following properties of the fluid and the particle are usually introduced, e.g. see Clift *et al.* (1978).

ρ_f density of the fluid phase,
ρ_p density of the dispersed phase,
μ_f viscosity of the fluid phase,
σ surface tension of the fluid particle interface layer,
d_e volume equivalent diameter of the particle,
Δu velocity difference between particle and fluid.

Although the last two parameters are not necessarily independent of each other, their introduction is common to define dimensionless groups of parameters that are customarily used to classify particulate two-phase flows and/or the motion of particles in fluids:

Reynolds number:
$$Re = \frac{\text{inertial force}}{\text{viscous force}} = \frac{\rho_f \Delta u \, d_e}{\mu_f},$$

Weber number:
$$We = \frac{\text{inertial force}}{\text{surface tension force}} = \frac{\rho_f (\Delta u)^2 d_e}{4\sigma},$$

Eötvös number:
$$Eo = \frac{\text{lift force}}{\text{surface tension force}} = \frac{g\Delta\rho \, d_e^2}{\sigma}.$$

Occasionally, another number is used:
Morton number:
$$Mo = Eo \, \frac{16 \, . \, We^2}{Re^4} = \frac{g\mu_f^4 \Delta\rho}{\rho_f^2 \, \sigma^3}.$$

Using the above dimensionless parameters, Clift *et al.* (1978) provided a diagram which correlates the shape of bubbles and drops with Re, Eo and Mo. This diagram is reproduced in figure 1.

It is somewhat surprising to see that the viscosity of the particulate phase does not appear in this diagram, nor do the dimensionless parameters commonly used to classify the motion of drops and bubbles in liquids. It is also worth noting that the description of the particle shape in figure 1 is somewhat imprecise; the so-called ellipsoidal shape refers to bubbles that are far from being symmetrical about a 'horizontal axis', although symmetry may exist about the vertical axis.

2.2. *Bubble shape*

The shape of rising bubbles and drops is determined by the pressure distribution along their interface layer and the shape is therefore defined by the mutual interaction of surface tension, viscosity, lift and inertial forces. Hence, investigations of shape should take into account the characteristic dimensionless numbers defined in §2.1. Pan & Acrivos (1968) reported analytical predictions of bubble and drop shapes for small Reynolds number ($Re < 1$) and also small Weber number ($We < 1$). High Re-number computations of bubble shapes have recently been presented by Harper (1972), Miksis, Vanden-Broeck & Keller (1982) and Auton (1984). Although all these computations seem to give good agreement with experiments under ideal experimental conditions, the predictions seem to fail when impurities which collect in the interface layer strongly influence the resultant bubble or drop shape. Surface contaminants reduce the mobility of the interface layer and thereby influence the velocity distribution inside and outside the particle, e.g. see Levich (1962). This in return results in an altered pressure distribution along the bubble or drop surface,
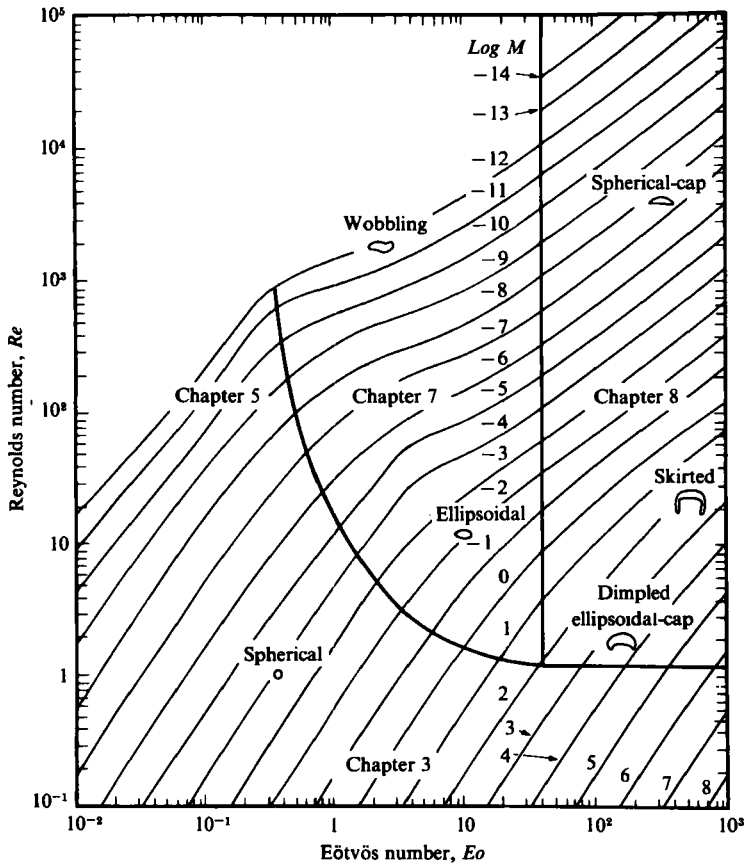
FIGURE 1. Shape regimes for bubbles and drops (reproduced from Clift *et al.* 1978).

giving an altered shape. Very little *quantitative* theoretical information exists on the effects of surface contaminants on the particle shape.

The shape and motion of fluid particles may also be influenced by the presence of the vessel walls in which they rise, especially if the vessel is too narrow. Among others Govier & Aziz (1972) have looked at this factor and have derived relationships for bubbles rising under laminar conditions in vertical tubes. They found that the following relationship,

$$\left(\frac{d_e}{D}\right)^{2.25} \ll 1,$$

must be valid for the presence of the pipe wall to have no influence on the particle motion.

2.3. *Flow field inside and around bubbles; rising velocity*

The distribution of streamlines, as assumed to exist inside rising bubbles and drops, is schematically shown in figure 2, see also Brauer (1982). Figure 2 also provides information on the velocity distribution along the horizontal centreline of bubbles or drops. Velocity distributions like this were computed by Hadamard (1911) and Rybczynski (1911) assuming low-Reynolds-number flow for both the inside and outside flow. With this assumption, simplified sets of partial differential equations
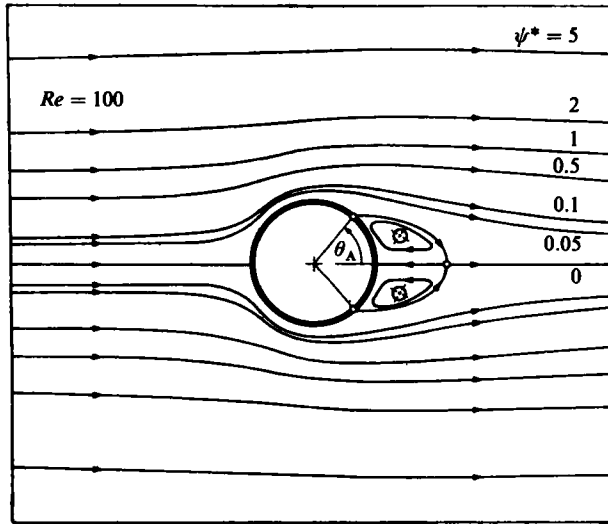
FIGURE 2. Streamlines of flow around a sphere (reproduced from Brauer 1982).

could be solved to yield the velocity distribution. To match the inside and outside solutions, the interface layer was assumed to be an 'ideal layer' i.e. the inside and outside flow exhibit the same shear stress at the interface layer.

On the basis of their computations, Hadamard (1911) and Rybczynski (1911) developed a formula for the terminal velocity u_T of gravity-driven particle motion in fluids. For gas bubbles in liquids their formula becomes:

$$(u_T)_{(2.1)} = \frac{g d_e^2 \rho_f}{12 \mu_f},$$ (2.1)

which differs from the Stokes' formula for creeping flow of rigid spheres

$$(u_T)_{(2.2)} = \frac{g d_e^2 \rho_f}{18 \mu_f}.$$ (2.2)

Experiments indicate that the terminal velocity of small bubbles obeys the Stokes' law rather than the formula derived by Hadamard (1911) and Rybczynski (1911). This suggests that the internal flow circulation of bubble or droplet motion very often does not occur for small-Reynolds-number flows. External vortex motion has only been observed for uncontaminated rising bubbles in liquids for $Re \gtrsim 100$. At high Eo numbers and small Re numbers, the motion is observed to be vertical and straight whereas helical upwards motion or plane zigzag motion occurs when the Eötvös number is decreased and/or the Reynolds number is increased.

It became apparent during the present study that little information exists on the flow around rising bubbles and drops for $Re \geqslant 1$. Theoretical studies are mainly concerned with small-Reynolds-number flows (e.g. see Hadamard 1911; Rybczynski 1911), or represent solutions of the basic equations of the fluid mechanics for the flow inside the rising particle only (e.g. see Durst, Schönung & Simons 1981; Harper 1972) with artificial prefixed particle shapes being employed. This lack of physical knowledge encouraged us to develop advanced experimental and theoretical means to study particulate two-phase flows and to apply these to air bubbles rising in liquids. Two

types of bubbles were selected that correspond to the low Eötvös-number and Reynolds-number range. These were selected to yield an upward motion with little deviation from a straight line, i.e. helical or zigzag motion was negligible.

3. Experimental investigations

This section summarizes the experimental work carried out to yield detailed fluid mechanics information on bubble-driven liquid flows together with information on the rise velocity of bubbles and the bubble shape. The work was carried out to extend the results obtained in a previous study by Durst, Taylor & Whitelaw (1984 a). A special test section with a bubble-generating nozzle was designed and built which allowed individual bubbles to be produced with frequencies up to $f_b = 2$ Hz. Around this test section, two laser-Doppler anemometers (LDA) were arranged to measure the fluid velocity u_f and the rising velocity u_b of the bubbles. The two systems were extended by two opto-electronic devices to yield information on the bubble shape and to identify the presence of a bubble in the measuring control volume. The latter device supported the signal processing system especially set-up for this study.

Section 3.1 provides details of the experimental test rig and the employed LDA-system. In §§3.2–3.4, information on the experimental results is given.

3.1. *Experimental test rig and LDA-system*

The experimental test rig is shown schematically in figures 3 (a)–(c). A top view and two side views are sufficient to explain the major features of the set-up. The actual test section consisted of a vertically mounted glass tube with an inside diameter of 100 mm. As figure 3 (a) indicates, the glass tube was surrounded by a square viewing box also made of glass. The space between the cylinder outer-wall surface and the glass window of the viewing box was filled with a mixture of octanol and castor oil adjusted to yield a liquid of the same refractive index as the wall material of the glass cylinder.

To carry out the experiments, two test liquids were used and details of their properties are given below:

Test liquid I: The first test liquid used was a mixture of octanol and castor oil. The volume ratio of the two components was adjusted so that the refractive index of the fluid matched that of the glass walls of the cylindrical fluid container. The same fluid also occupied the space between the viewing box inner surface and the outer surface of the tube. In this way, a distortion-free laser beam pass was achieved for the LDA-measurements with test liquid I.

Prior to the experiments, the following characteristic parameters of the fluid were obtained and remained constant during the experiment:

refractive index:
$$n = 1.470,$$

dynamic viscosity:
$$\mu_f = 330 \text{ cP} = 0.33 \text{ kg/ms (at 24.4 °C)},$$

surface tension:
$$\sigma = 0.036 \text{ N/m},$$

density:
$$\rho_f = 810 \text{ kg/m}^3.$$

These quantities yield the following characteristic dimensionless numbers for the bubbles in the first set of experiments:

$$Re = 1.7; \quad Eo = 11.3 \quad \text{and} \quad Mo = 3.1.$$

Test liquid II: In the second set of experiments, a test liquid consisting of a mixture of water and glycerin with a volume ratio of 1:1 was used. With this mixture, a combination of dimensionless numbers was obtained such that the resultant bubbles show a straight upward, zigzag-free motion. This greatly facilitated the performance of the experiments but did not permit the refractive index of the test liquid to be matched to that of the glass walls of the test section. Because of this, the measuring position could not be taken from the readings of the position indicator of the traverse table but had to be corrected within the data processing procedure.

The following characteristic parameters of test liquid II were obtained and remained constant during the experiments: ·

refractive index:
$$n = 1.4085,$$

dynamic viscosity:
$$\mu_f = 8.333 \text{ cP} = 8.333 \times 10^{-3} \text{ kg/ms (at 20 °C)},$$

surface tension:
$$\sigma = 0.053 \text{ N/m},$$

density:
$$\rho_f = 1136 \text{ kg/m}^3.$$

With these parameters, the following characteristic dimensionless numbers were achieved for the bubbles used in the second set of the experiments.

$$Re = 64; \quad Eo = 0.927; \quad Mo = 2.8 \times 10^{-7}.$$

The properties of the above test liquids were carefully chosen to meet experimental requirements imposed by the LDA-measuring technique and at the same time, to ensure bubbles with ellipsoidal shape and vertically straight upward motion.

The cylindrical test section with viewing box was built as an integrated test rig, the bottom part of which consisted of a precision made air-supply nozzle together with the air control devices preceding the nozzle. This permitted fine air-supply adjustments to be made so that the supply stability was better than 2 % during each experiment. This stability was continuously checked during the experiments by recording the resultant bubble frequency.

In order to permit traverses of the entire velocity field, the integrated test rig was mounted on a three-dimensional traversing arrangement which permitted movement of the test section in three orthogonal directions relative to the spatially fixed LDA-optical units. The other LDA-optical unit was fixed to the test section traverse but an additional traverse arrangement was available which made it possible to position the measuring volumes of two LDA-systems independently of each other in any locations inside the circular cylinder test section. Traverses up to 550 mm above the nozzle upper surface were possible with this set-up.

As already mentioned, the velocity measurements were made with two different LDA-systems, one for the measurements of the liquid velocity and one for the bubble rise velocity. The former of these consisted of a forward-scattering anemometer, whose physical principles of operation are given by Durst, Melling & Whitelaw (1976). Its lay-out is divided into two parts, the emitting and the collecting optics, with a measuring volume inside the fluid test section, between the two optical parts.
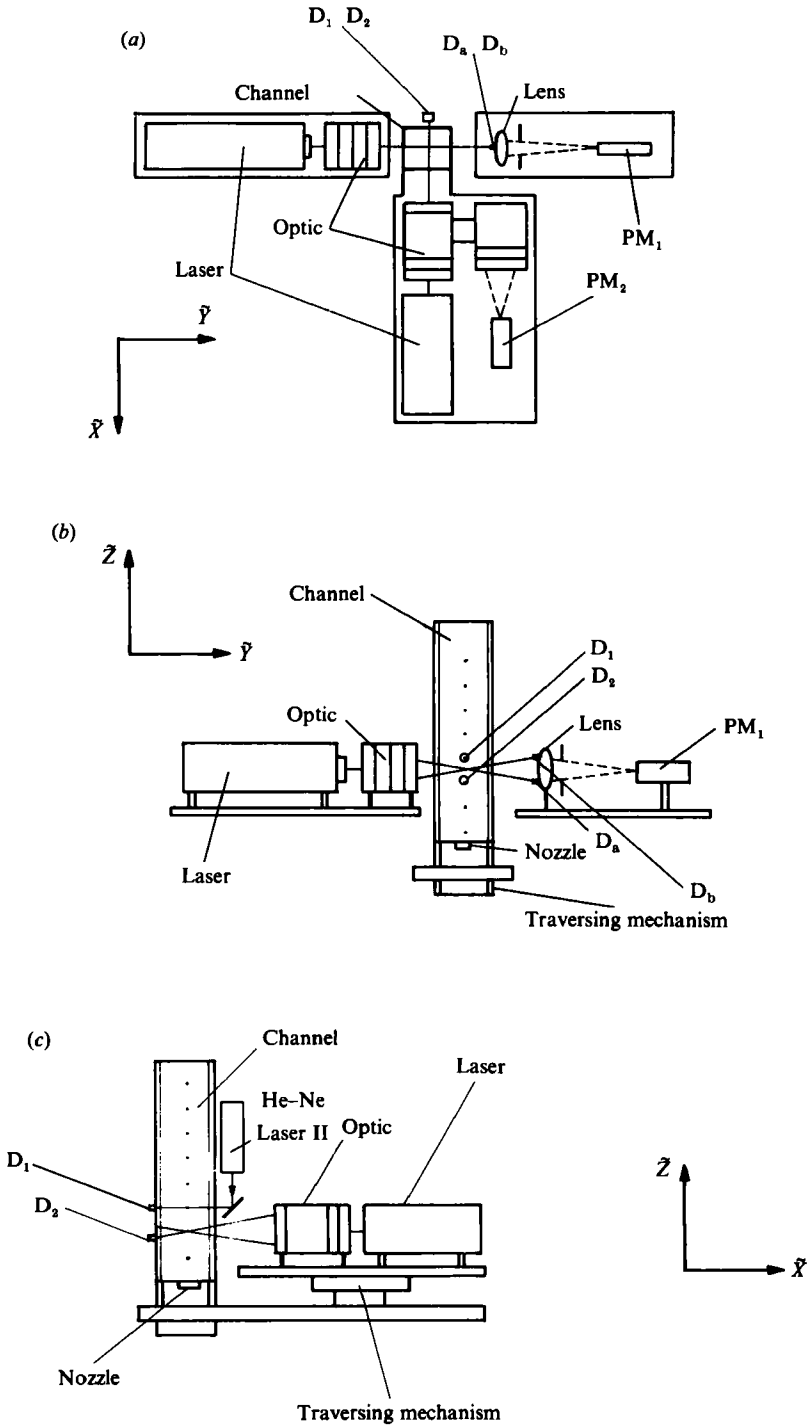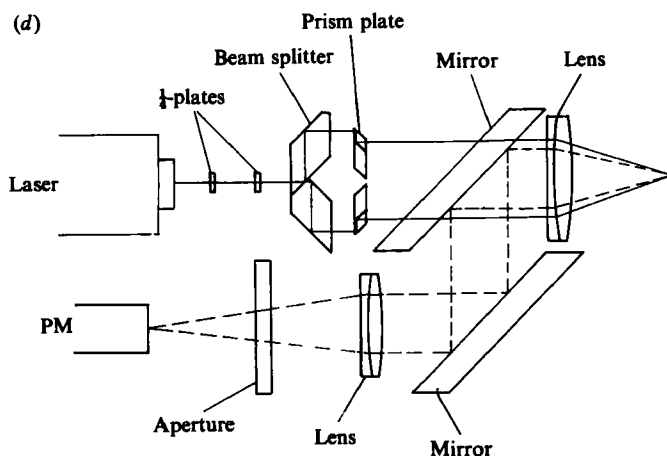
FIGURE 3 (*a–c*). For caption see facing page.

FIGURE 3. (*a*) Test rig (top view). (*b*) Forward scattering anemometer (side view). (*c*) Back-scattering anemometer (side view). (*d*) Details of the back-scattering Laser-Doppler anemometer.

The emitting optics of the forward-scattering system, see figures 3 (*a*) and (*b*), consisted of a 15 mW helium–neon laser ($\lambda = 632.8$ nm), a polarization rotator, a beam-splitter prism, two Bragg cells and a 250 mm focusing lens. An integrated optical unit, greatly simplified the beam alignment procedure. The entire optical system was rotatable around its optical axis, permitting the horizontal and vertical velocity components to be measured. The frequency shift performed by the Bragg cells made it possible to distinguish between the positive and negative directions of the flow. In this way, regions of the flow with small or even zero velocity could also be investigated.

The characteristics of the forward-scattering LDA-system were:

(i) half angle between intersecting laser beams:

$$\phi = 5.7°,$$

(ii) 'fringe' spacing inside measuring volume:

$$x = \frac{\lambda}{2 \sin \phi} = 3.2 \ \mu\text{m},$$

(iii) measuring volume dimension in flow direction:

$$2s = \frac{2\lambda f}{\pi r_w} = 220 \ \mu\text{m},$$

where $r_w = 0.45$ mm was the waist $1/e^2$-radius of the laser beam at the front laser mirror.

On the collecting side, the optical system consisted of a 150 mm lens which imaged a 150 μm pinhole, located in front of the photomultiplier – with an optical imaging ratio of $1:1$ – into the measuring control volume.

The bubble rise velocity was measured by a back-scattering anemometer extended for two-phase flow measurements as suggested by Durst & Zaré (1975) and Martin *et al.* (1981). The light source was a 5 mW He–Ne laser. The main parts of the optical unit are two $\frac{1}{4}\lambda$ plates, a beam splitter, a beam separation adjustment unit, a 400 mm focusing lens and two mirrors (see figure 3*a*–*d*). With this system, the same lens is

used to focus the two laser beams of the transmitting optics and to collect the light reflected from the interface layer of the rising bubbles. In order to yield high signal modulations, the optics incorporated a pinhole aperture arrangement as described by Martin *et al.* (1981). In this way, a single amplitude discriminator ensures that only bubble signals are detected.

The characteristics of the back-scattering optical systems were:

(i) half angle between intersecting laser beams:

$$\phi = 3.7°,$$

(ii) 'fringe' spacing inside measuring volume:

$$x = \frac{\lambda}{2\sin\phi} = 4.928 \ \mu\text{m},$$

(iii) measuring volume dimensions in flow direction:

$$2s = \frac{2\lambda f}{\pi r_w} = 220 \ \mu\text{m},$$

where $r_w = 0.65$ mm was the waist $1/e^2$-radius of the laser beam.

In order to separate bubble signals from signals resulting from small particles inside the fluid, additional opto-electronic devices were incorporated in the LDA-systems. The undisturbed light path of the two laser beams of the forward-scattering anemometer was monitored by a pair of photodiodes, shown in figures 3(*a*) and (*b*) as D_a and D_b. Each time, a bubble traversed the measuring volume, the pair of photodiodes were interrupted and this resulted in a gate signal of $U_{ab} = -12$ V. If the bubble velocity u_b is assumed to be constant within this gate time, the duration t_{ab} of the gate signal becomes a direct measure of the bubble extension in the direction of the bubble motion. Knowing the bubble velocity, and measuring the time during which the bubble is present inside the measuring control volume, permitted the bubble shape to be evaluated from gate measurements at various location around the axis of the tube test section.

Two additional photodiodes were incorporated into the optical system, indicated as D_1 and D_2 in figures 3(*a*)–(*c*). For every bubble passage, these photodiodes gave a start and stop pulse that defined a time window over which LDA-measurements were made for one bubble passage. The positions of the photodiodes D_1 and D_2 were readjusted with increasing frequencies of the generated bubbles. Within the start–stop pulses of D_1 and D_2, a gate voltage of $U_{12} = +12$ V was available as information to the signal processing system.

The actual signal processing scheme is sketched in figure 4. The fluid signal line consisted of a photomultiplier followed by an additional amplification stage, a band-pass filter and a BBC-Görtz frequency-tracking demodulator (frequency tracker). The analog output of this tracker was amplified and filtered and overlaid with the gate voltage produced by the two photodiodes D_a and D_b, i.e. with a voltage of $U_{ab} = -12$ V. This signal was digitized and stored in an HP-1000 computer. This computer also stored the gate signal for individual bubbles, i.e. $U_{12} = +12$ V.

The laser-Doppler signal from the interface of the rising bubbles was handled in a second branch of the signal processing electronics. The signal from a photomultiplier (PM2) was amplified, filtered and then digitized and stored by a Datalab (Model DL 922) transient recorder. The stored and digitized signals were also supplied to the HP-1000 computer where software programs were available to check the quality of
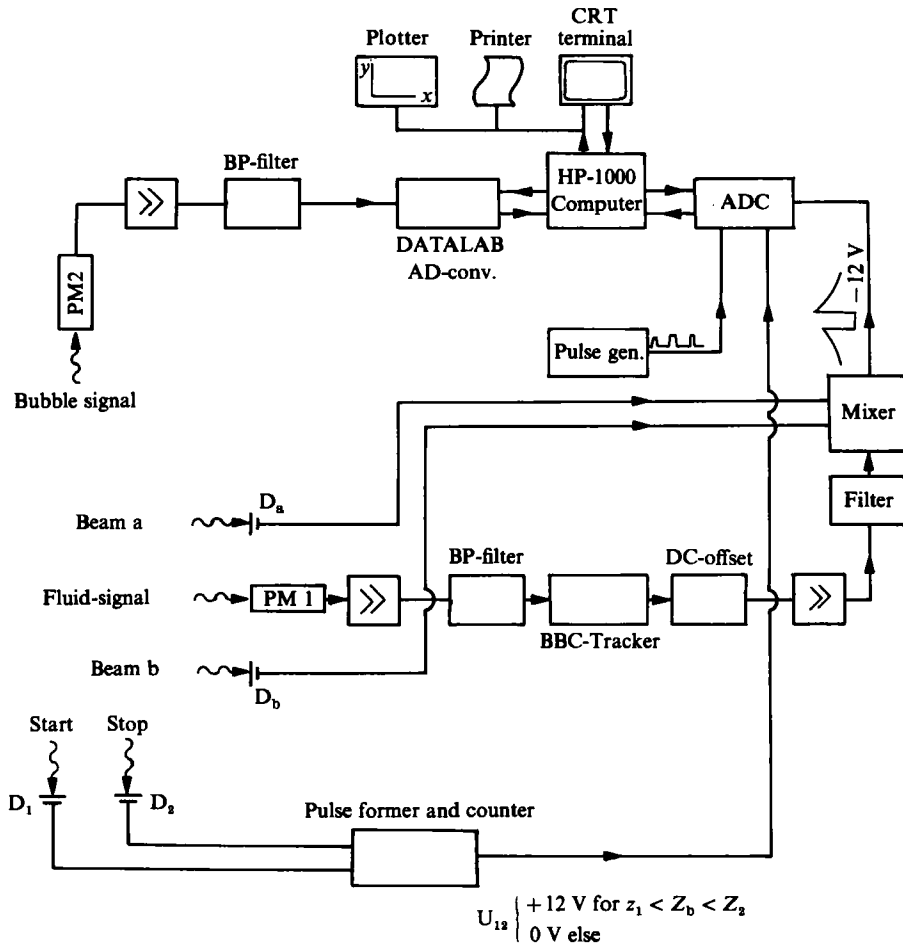
FIGURE 4. Signal processing scheme.

the resultant Doppler signals prior to evaluating the Doppler frequency, and from it the bubble rise velocity. Due to the various time delays in the digitization and signal storage phases of this branch of the signal processing system, signal timing became an important part of the data processing in the HP-1000 computer.

The optical and electronic system described above yielded information on the instantaneous fluid velocity and the bubble rise velocity. These data were used to compute the various pieces of information on bubble-driven liquid flows provided in the following sections. At each position in the flow ensemble averages were measured for the velocities and the gate times and these averages are used below.

3.2. *Flow around bubbles and bubble shapes*

The bubble rise velocity was measured by the backscatter LDA-system and yielded the results given in table 1. For increasing bubble frequency the data show the expected slight increase in the bubble rise velocity typical for low frequency bubble chains rising in a fluid of high viscosity. Extrapolating the above rise velocity to $f_b = 0$ yields the following terminal velocities:

$$(u_T)_I = 85.5 \text{ mm/s}, \quad (u_T)_{II} = 208 \text{ mm/s}.$$

Test liquid I				Test liquid II		
f_b [Hz]	u_b [mm/s]	T [°C]		f_b [Hz]	u_b [mm/s]	T [°C]
0.166	86.7	24.5°		0.333	211.7	18°
0.366	87.9	24.5°		0.517	215.8	21°
0.633	89.7	24.5°		0.633	215.4	17.9°
0.917	89.5	24.3°		0.833	216.9	18°

TABLE 1

This terminal velocity has to be seen in connection with the measured bubble shape, given in figures 5(a) and (b), yielding the following volume equivalent bubble diameters:

$$(d_e)_I = 6.56 \text{ mm}, \quad (d_e)_{II} = 2.08 \text{ mm}.$$

This permits the theoretical terminal velocity to be computed for test liquid I using (2.1) and (2.2):

$$(u_T)_{(2.1)} = 86 \text{ mm/s}, \quad (u_T)_{(2.2)} = 58 \text{ mm/s}.$$

A comparison with the measured quantities shows that the measured terminal velocity is closer to the value computed by (2.1) and this suggests that internal circulation was present in the bubbles studied with test liquid I. For test liquid II, correctly speaking, neither (2.1) nor (2.2) can be used because the Reynolds number is too high ($Re \approx 65$). However, internal circulation is likely to be present for this sphere also, because for a rigid sphere with the same density the terminal velocity would be only $u_T = 120$ mm/s.

The liquid flow around the rising bubbles was measured locally with the forward-scattering LDA-system. Utilizing the above rise velocity allowed the data to be plotted and tabulated with reference to a coordinate system attached to the corresponding bubble. In this way, information on the flow field, as indicated in figures 5(a) and (b) and 6(a–d), was obtained. These figures show examples of plots of the measured velocity fields that indicate that no clearly identifiable separated flow regions occurred behind the bubbles. This can be taken as another indication that internal flow circulation was present for both bubble motions studied. A solid sphere, at the higher Reynolds number of the two sets of bubbles, would have shown flow separation.

3.3. Bubble-driven liquid flow

The measured distribution of liquid velocity across the entire test section, at a height where the bubbles had reached a stationary rise velocity, is given in figures 7(a) and (b). The continuity equation checks well for the upward and downward flow and this check confirms the accuracy of the velocity data to be better than ± 0.1 mm/s. This accuracy is also confirmed by the low scatter of the data indicated in figure 8 which gives an example of a detailed plot of the time-averaged vertical velocity component, measured for test liquid I. Figure 8 indicates that the time-averaged fluid velocity profile is nearly flat in the centre part of the test section and tends to fall off rapidly from the point where the bubbles have reached their maximum horizontal dimension.

Figure 9 provides further information on the bubble-driven liquid motion for test liquid I. It shows the time-averaged velocity $u_f(r = 0)$ on the axis of the cylindrical test section and at a height where this velocity has become independent of the
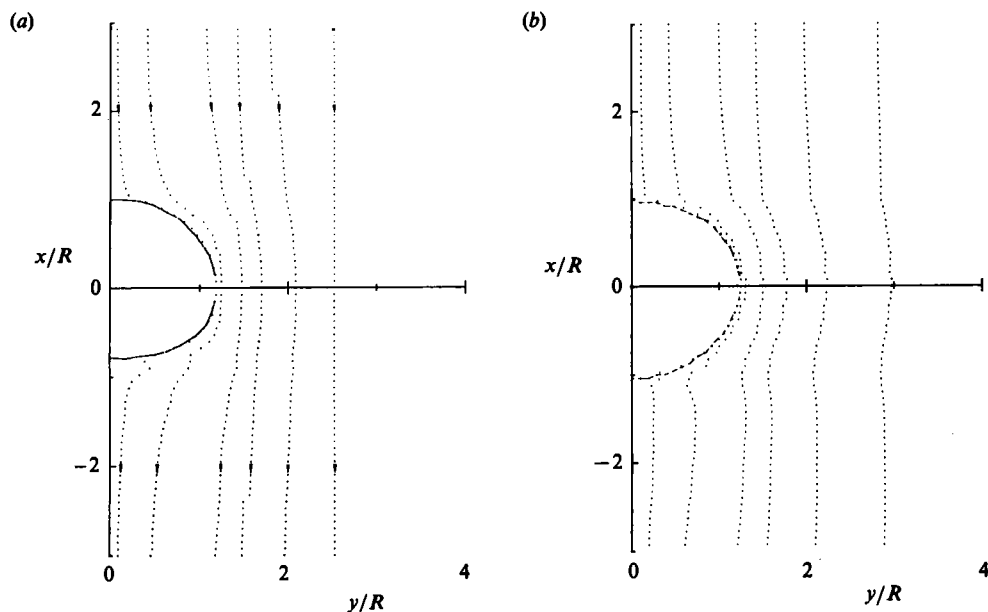
FIGURE 5. (a) Streamlines around a bubble (test liquid I). $Re = 1.8$; frequency $= 0.633$ Hz.
(b) Streamlines around a bubble (test liquid II). $Re = 63.9$; frequency $= 0.633$ Hz.

distance from the nozzle exit. This figure also contains information on the upward liquid flow rate Q_f. Both quantities are plotted as a function of the bubble frequency and reveal a surprising feature of the liquid motion. Although for $f_b = 0.667$ Hz, the rising bubbles were already so closely spaced that the liquid velocity on the axis moved continuously between bubbles, the relationship between Q_f and $u_f(r = 0)$ and the bubble frequency still remained linear up to $f_b = 1.917$ Hz, the highest frequency studied.

Measurements of liquid and bubble velocity were also performed for test liquid II. No particular differences to the measurements of test liquid I were obtained. However, in order to obtain accurate measurements of the fluid velocity distributions for the experiments with test liquid II, the room temperature had to be closely controlled and maintained at a value almost the same as the temperature of the test liquid. Otherwise, buoyancy-driven liquid motions occurred, observable as thin rising liquid films near the wall of the cylinder. Furthermore, the height the bubbles had to travel to obtain a constant rise velocity, was longer for test liquid II than for test liquid I. Consequently, position-independent liquid-velocity profiles could only be measured over a reduced region away from the nozzle. Using test liquid II, the velocity showed strong variations with time if no particular care was taken to cover the top of the cylindrical test section. This was found accidentally and in the first sets of experiments caused us to take great care to obtain time-independent flow fields. In a second set of studies, the cause of the time variations of the flow field was studied in detail, both experimentally and theoretically. The outcome of the studies is given below.

3.4. *Bubble velocity variations along the bubble path*

The investigations described in this section were performed after accidental observations showed, especially for test liquid II, that variations occurred in the results of

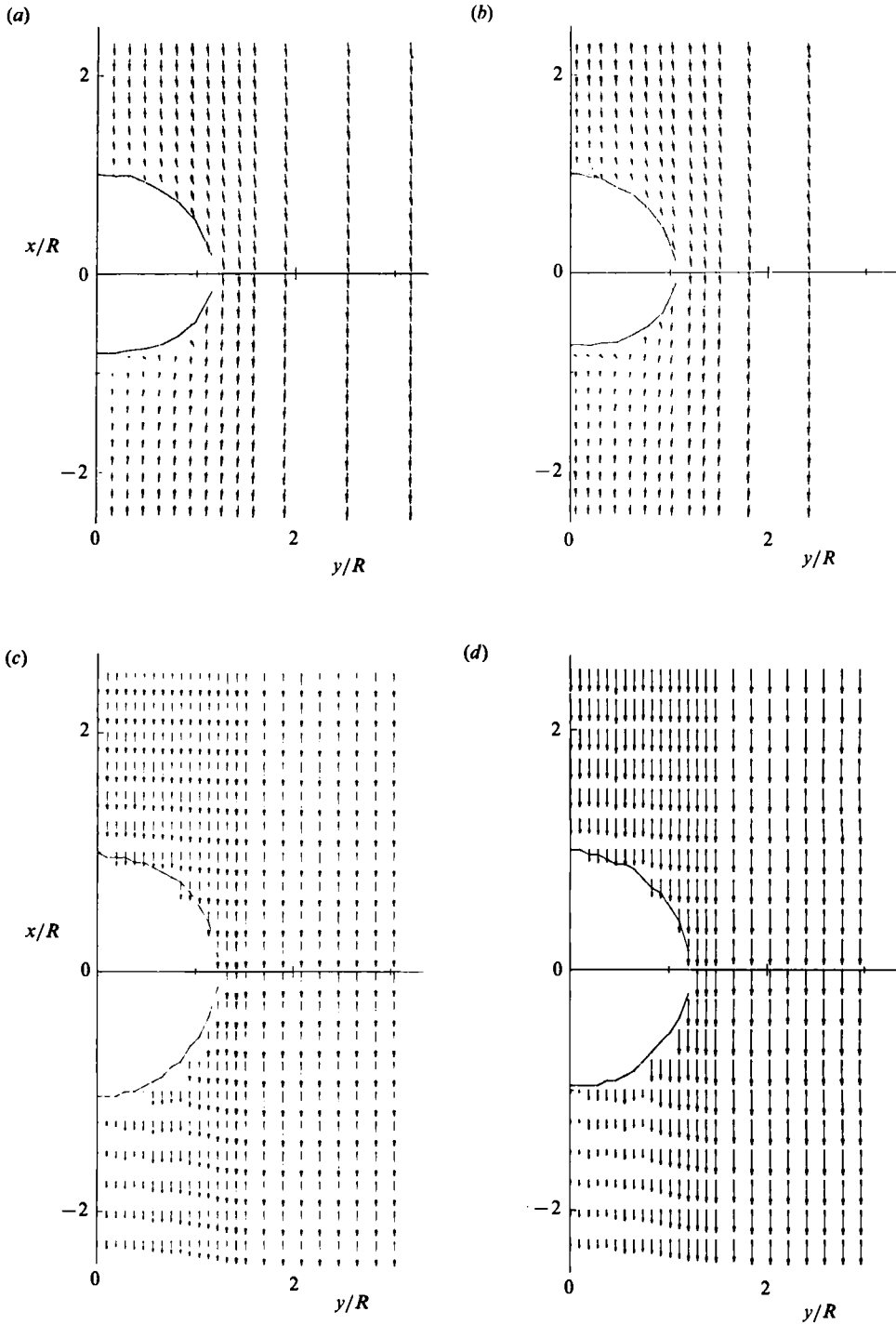*F. Durst, B. Schönung, K. Selanger and M. Winter*

FIGURE 6. Velocity fields at two different frequencies. Test liquid I: (a) $Re = 1.73$; frequency = 0.166 Hz. (b) $Re = 1.76$; frequency = 0.366. Test liquid II: (c) $Re = 63.9$; frequency = 0.633 Hz. (d) $Re = 63.8$; frequency = 0.883 Hz.
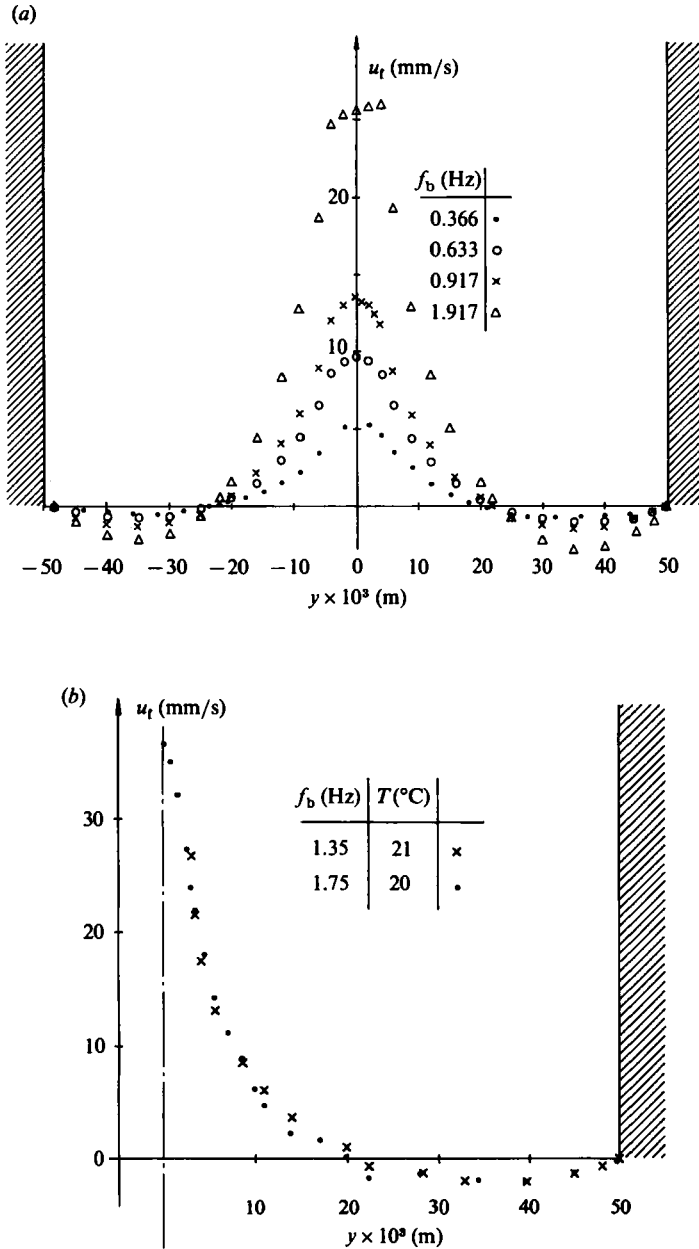
FIGURE 7. (*a*) Liquid velocity across the test section (test liquid I). (*b*) Liquid velocity across the test section (test liquid II).

liquid-velocity measurements carried out on different days. Results of bubble-velocity measurements showed corresponding differences along the bubble path, i.e. the centreline of the pipe test section, and these are shown in figure 10. This diagram indicates that close agreement was obtained for all results in the lower part of the test section, i.e. for about 70 mm above the bubble-producing nozzle. Thereafter the bubble velocity did not remain constant at the level of the terminal velocity, but showed a characteristic decrease with height. As figure 10 shows, the slope of
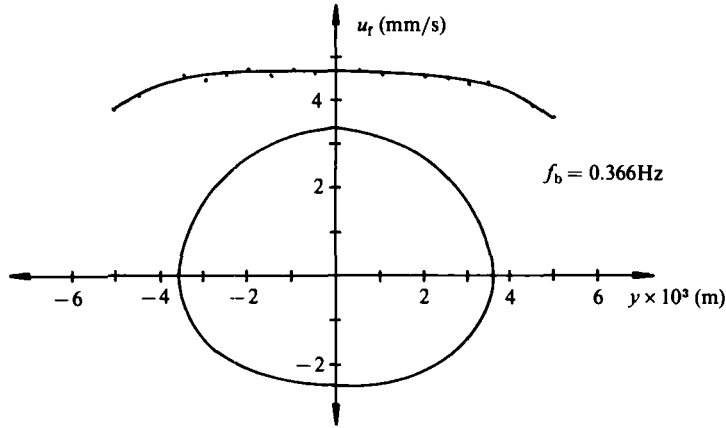
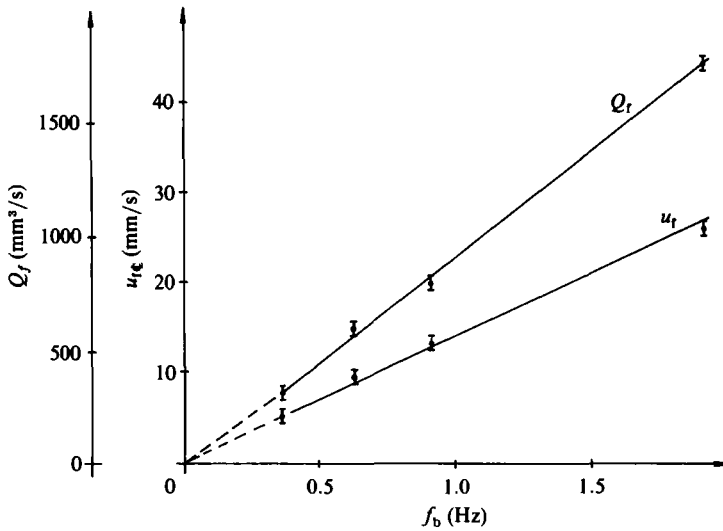FIGURE 8. Core flow profile for test liquid I and bubble shape.

FIGURE 9. Mean upward liquid flow rate Q_f and liquid centreline velocity as function of the bubble frequency.

decrease in the bubble-rise velocity increased with time. After reaching a velocity maximum, the bubble-rise velocity continuously decreased with height. This readily suggested that impurities entered the test liquid through the open end of the pipe test section and these caused the well-known 'stiffening' of the gas–liquid interface. As time went on, more impurities were able to enter the test liquid causing a faster collection of impurities in the gas–liquid interface. The amount of non-liquid interface substances also increased with height and this caused the continuous decrease of bubble velocity with distance from the bubble-producing nozzle.

Increasing the impurity content in test liquid II caused an asymptotic velocity variation with distance from the nozzle to be reached. This variation is shown in figure 11 for different liquid heights. It was assumed that this asymptotic velocity versus height-distribution was reached due to the diffusion limited transport of impurities to the gas–liquid interface of the bubble. Because of this, there is a limited
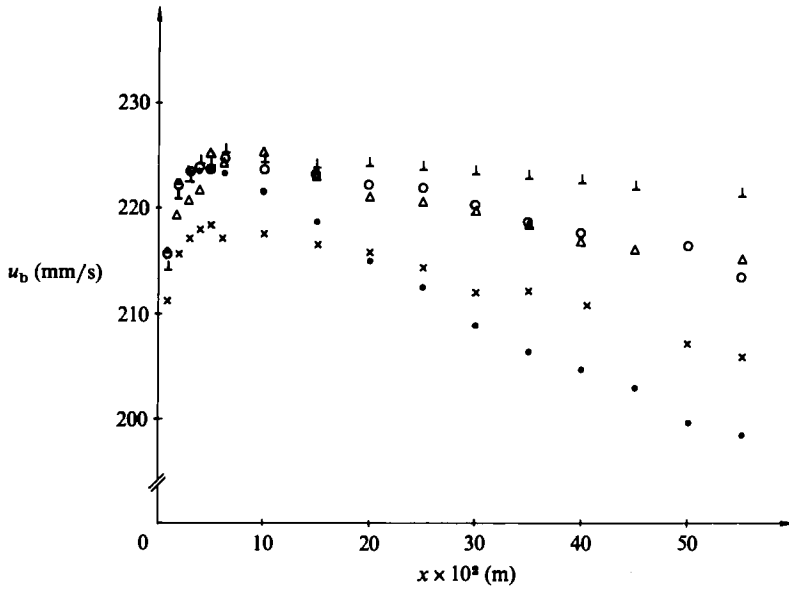
FIGURE 10. Bubble velocity at different liquid age. $\perp$, 24.5.83, $T = 20.5$ °C; $\triangle$, 25.5.83, $T = 20$ °C; $\bigcirc$, 26.5.83, $T = 20.3$ °C; $\times$, 27.5.83, $T = 19.8$ °C; $\bullet$, 7.6.83, $T = 22.6$ °C.
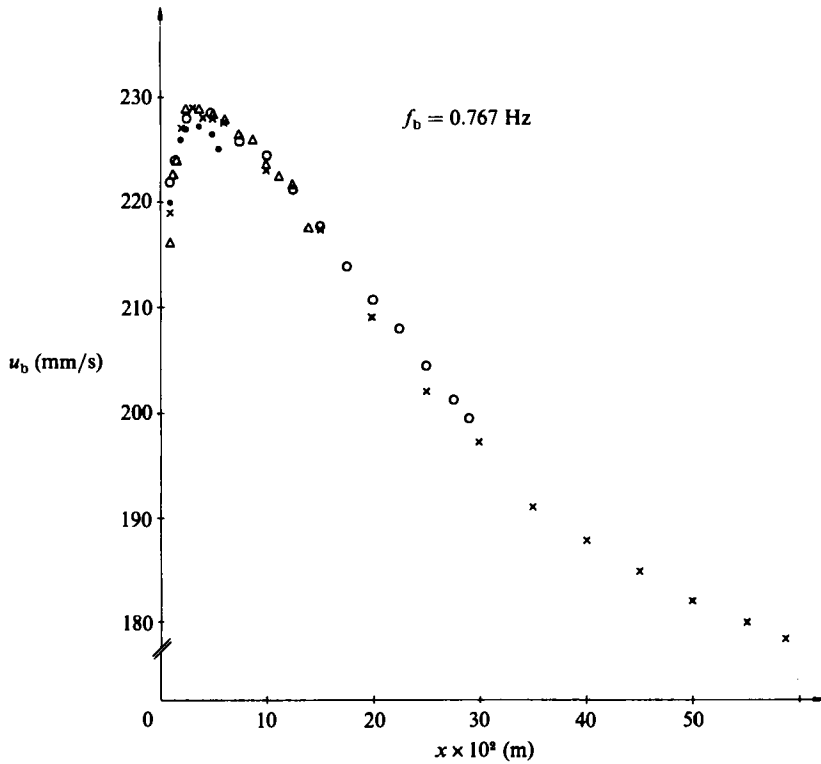

FIGURE 11. Bubble velocity at different liquid heights. $\times$, $H = 0.6$ m; $\bigcirc$, $H = 0.3$ m; $\triangle$, $H = 0.15$ m; $\bullet$, $H = 0.072$ m.

value for the rate at which the impurity concentration in the interface of the bubble can change, irrespective of the outside concentration. This is clearly reflected by the results in figure 11. Hence, for any kind of particle–liquid system there will be a characteristic bubble velocity versus height distribution which applies to high impurity concentrations and characterizes the diffusion-controlled stiffening of the bubbles due to concentration increase of impurities in the bubble interface. It is characteristic that the bubble-rise velocity will show a maximum a short distance above the bubble-generating nozzle. In this region, there will be a maximum of mass transfer from the bubble to the liquid, as already indicated in the recent measurements of Brankovic, Börner & Martin (1984).

4. Theoretical investigations

4.1. *Basic equations and their numerical solution*

Bubble-driven liquid flows, as described in the previous chapters, are among the most simple types of dispersed two-phase liquid–gas flows. For flows of this kind, basic equations are available to deal theoretically with the motions of the dispersed and the continuous fluid and many attempts to yield solutions to these equations are described in the literature.

To predict the liquid flow induced by a line of subsequently rising bubbles, it is general practice to solve the continuity and momentum equations for the liquid flow around upward moving spheres located along the axis of a cylinder. If this approach is chosen, time dependent partial differential equations need to be solved for very complex boundary conditions; these boundary conditions are time dependent if the coordinate system is chosen to be fixed in space. Under these conditions the boundary conditions on the bubble–liquid interface are the most difficult to impose on the partial differential equation.

Because of the aforementioned difficulties, the present theoretical treatments relied on a different approach to yield information on bubble-driven liquid flows. The predictions are based on the Eulerian approach, which assumes that the dispersed phase can be treated as a continuum. The continuity and momentum equations for both phases are derived and interaction terms that express the transfer of momentum, mass, and energy between the two phases are included. These interaction terms have to be modelled locally, and in general analytically or experimentally gained correlations for simple flow configurations are used to close the resultant set of partial differential equations.

To formulate the two-phase flow equations in this way requires a local void fraction to be introduced:

volume-concentration of phase k $\alpha_k = \dfrac{V_k}{V}$,   (4.1)

where $V_k \triangleq$ volume occupied by phase k, $V \triangleq$ total volume. Taking into account that the following relationship holds:

$$\alpha_b + \alpha_f = 1,$$

allows the continuity and momentum equations for both phases to be written in the following form, e.g. see Schönung (1983), Durst, Milojevic & Schönung (1984b), ($k = f$, fluid phase; $k = b$, bubble phase),

continuity equation:

$$\frac{\partial}{\partial x}(\alpha_k \rho_k u_k) + \frac{1}{y}\frac{\partial}{\partial y}(y\alpha_k \rho_k v_k) = 0,$$ (4.2)

momentum equations:

x-direction:

$$\frac{\partial}{\partial x}(\alpha_k \rho_k u_k^2) + \frac{1}{y}\frac{\partial}{\partial y}(y\alpha_k \rho_k u_k v_k) = -\alpha_k \frac{\partial p}{\partial x} + 2\frac{\partial}{\partial x}\left(\alpha_k \mu_k \frac{\partial u_k}{\partial x}\right)$$

$$+ \frac{1}{y}\frac{\partial}{\partial y}\left(y\alpha_k \mu_k \left(\frac{\partial u_k}{\partial y} + \frac{\partial v_k}{\partial x}\right)\right) + \Phi_{k,x} + F_{k,x}, \quad (4.3)$$

y-direction:

$$\frac{\partial}{\partial x}(\alpha_k \rho_k u_k v_k) + \frac{1}{y}\frac{\partial}{\partial y}(y\alpha_k \rho_k v_k^2) = -\alpha_k \frac{\partial p}{\partial y} + \frac{2}{y}\frac{\partial}{\partial y}\left(y\alpha_k \mu_k \frac{\partial v_k}{\partial y}\right)$$

$$+ \frac{\partial}{\partial x}\left(\alpha_k \mu_k \left(\frac{\partial u_k}{\partial y} + \frac{\partial v_k}{\partial x}\right)\right) - 2\alpha_k \mu_k \frac{v_k}{y^2} + \Phi_{k,y}. \quad (4.4)$$

The underlined terms are zero for the dispersed phase in a laminar flow and the following forces acting on the liquid and gas phases are included:

gravity:

$$F_{f,x} = -\beta g \rho_f, \quad F_{b,x} = -\alpha g \rho_b, \quad (4.5)$$

drag:

$$\Phi_{b,x} = \tfrac{3}{4}\alpha\beta c_D \frac{\mu_1}{d^2} Re_p \Delta u, \quad \Phi_{f,x} = -\Phi_{b,x}, \quad (4.6)$$

$$\Phi_{b,y} \quad \Phi_{f,y} \quad \text{analogous}.$$

The above set of partial differential equations needs to be solved for the boundary conditions that characterize the two-phase flow under investigation. For the bubble-driven liquid flow studied here, the boundary conditions were:

inlet:

$$u_f, \quad u_b, \quad \alpha, \quad \text{prescribed}, \quad (4.7)$$

exit:

$$\left.\begin{aligned} u_f &= 0, \\ \frac{\partial \Phi}{\partial x} &= 0, \quad \Phi = u_b, v_f, v_b, \alpha, \end{aligned}\right\} \quad (4.8)$$

symmetry-line:

$$\left.\begin{aligned} v_f &= v_b = 0, \\ \frac{\partial u_f}{\partial y} &= \frac{\partial u_b}{\partial y} = \frac{\partial \alpha}{\partial y} = 0, \end{aligned}\right\} \quad (4.9)$$

wall:

$$u_f = v_f = 0. \quad (4.10)$$

It has to be emphasized that, for the predictions, only the mass flow rate of the two phases (see (4.7)) at the inlet and the size of the bubbles have to be prescribed (see (4.13)). The volume concentration of the gas and the velocity of both the phases are calculated in the whole domain by solving equations (4.2)–(4.10). For the predictions of Durst *et al.* (1984*a*), the fluid velocity along the axis of the cylinder had to be prescribed as a boundary condition and only single-phase flow calculations were performed to get the fluid velocity distribution.

The partial differential equations (4.2)–(4.4) are solved by using the appropriate finite difference equations, derived by integrating the differential equations over

control volumes, e.g. see Schönung (1983). For this purpose an orthogonal grid is applied, for which the two velocity components for each of the phases and the pressure are stored in staggered-grid positions. The necessary linearization of the non-linear equations is performed by hybrid differences to get an implicit finite difference scheme. Because of the elliptic nature of the partial differential equations, an iterative-solution procedure needs to be employed to yield solutions. Starting with guessed distributions of the velocity and pressure fields, the fluid velocities are calculated from the momentum equations. Thereafter, the solution of a pressure correction equation (Poisson equation), which has been derived from the continuity equation, yields corrected values for the velocity and the pressure fields so that the continuity equation is satisfied. With the corrected values, the momentum equations are solved again and the whole procedure is repeated until convergence is achieved.

The integration of the partial differential equations (4.2)–(4.4) requires the unknown momentum interaction terms $\Phi_{k,x}$ and $\Phi_{k,y}$ to be modelled. As shown below, this is equivalent to prescribing a drag coefficient for the bubble motion. If the fluid–particle interaction is more complex, e.g. if there is mass or heat transfer between the two phases, the interaction terms need to be modified to yield correct particle and fluid flow predictions through the employed theoretical approach.

4.2. *Treatment of particle–fluid interaction*

The bubble-driven liquid flow studied in this paper is characterized by bubbles rising along the centreline of a circular test section; the resultant flow is axisymmetric. Under these conditions, a single interaction force results acting in the direction of the bubble motion. It is usually referred to as buoyancy or drag force depending on whether it is considered to act on the bubble stream or on the fluid. Its magnitude can be expressed in terms of a drag coefficient. For bubble flows, the drag coefficient depends on various parameters and in §2 the main ones have already been given expressed in the form of dimensionless numbers like: Reynolds number Re, Weber number We, Eötvös number Eo, and Morton number Mo. It has also been shown in §2 that surface contamination (see Martin & Chandler 1982), can have a strong influence on the resultant terminal velocity, i.e. on the resultant bubble drag coefficient. Another strongly influencing parameter is the bubble shape, which was close to spherical in our experimental studies. Hence, the present theoretical consideration concentrates on spherical bubbles only.

For creeping flow ($Re < 1$), some analytically derived correlations for the drag coefficient C_D as a function of Reynolds number Re have been obtained for solid spheres (Stokes 1891, Oseen 1927; and Goldstein 1929). For bubbles without surface contamination, the corresponding correlations can be deduced from the analytical treatment of bubble motion as carried out by Hadamard (1911) and Rybczynski (1911) (see §2.3).

At larger Reynolds numbers ($Re > 1$), the non-linear terms in the Navier–Stokes equations, usually neglected in analytical treatments of particle motion or only accounted for approximately, cannot be neglected; they need to be considered in deriving analytically $C_D - (Re)$-correlations. This requirement makes analytical derivation of drag coefficient Reynolds-number relationships difficult and forces theoretical treatments of bubble-driven liquid flows to rely on experimentally obtained $C_D - (Re)$-correlations. For solid spheres it is found that the following relationship:

$$C_D = \frac{24}{Re}(1 + 0.15\,Re^{0.687}) \quad (Re \leqslant 1000), \tag{4.11}$$

is a satisfactory correlation for the so-called standard drag curve for solid spheres. The corresponding relationship for the drag coefficient of rising bubbles with 'clean' interfaces can be written as (see Clift *et al.* 1978):

$$C_D = \frac{14.9}{Re^{0.78}} \quad (Re > 2). \tag{4.12}$$

The difference between (4.11) and (4.12) is due to the presence of the fluid circulation inside bubbles and the corresponding differences in the motion of the fluid around the bubble. It is found, however, that very great care has to be taken to obtain experimental data for rising bubbles that are in agreement with (4.12). Small amounts of impurities in the test liquid already result in C_D-values that lie between those predicted by (4.11) and (4.12). This indicates that even for most laboratory studies of liquid-driven bubble flows, interface active impurities are present and need to be taken into account in theoretical treatments of the flow. This finding is considered in §4.5.

4.3. *Predictions of fluid motion*

Employing the solution procedure for the finite difference equations given in §4.1, and using the correlation for the drag coefficient of rising bubbles given in §4.2, predictions of the time-averaged fluid motion were made.

4.3.1. *Numerical prediction of the elliptic, recirculating liquid flow*

As the liquid flow field in the vertical cylinder is elliptic, the whole set of equations (4.1)–(4.10) has to be solved iteratively. At the inlet the rising velocity of a bubble with diameter d_e has been prescribed as the inlet velocity of the gas phase. Assuming a step function for the gas volume concentration (see (4.14)) and taking into account,

$$\int_0^{\frac{1}{2}D} \alpha(y)\, y \, dy = \alpha_0 \cdot \frac{d_e^2}{8} = \frac{1}{12} \frac{f_b d_e^3}{u_b}, \tag{4.13}$$

the inlet conditions for the gas phase can be written as:

$$\alpha = \begin{cases} \alpha_0 & (y < \tfrac{1}{2}d_e), \\ 0 & (y \geqslant \tfrac{1}{2}d_e), \end{cases} \qquad u_p = \begin{cases} u_b & (y < \tfrac{1}{2}d_e), \\ 0 & (y \geqslant \tfrac{1}{2}d_e). \end{cases}$$

For all the calculations a grid with 42×42 points (42×6 grid points in the bubbly region) has been used. The predictions are regarded as converged if the residuum of the continuity equation, normalized with the bubbly mass flow rate, is smaller than 10^{-3}.

In figure 12 a typical streamline distribution ($\psi^* = \psi/\psi_{\max}$) is presented for test liquid I and for a bubble frequency $f_b = 0.917$ Hz.

The streamlines show similar shapes near the bottom and the top surface of the liquid container. Parallel, vertical streamlines result over most of the cylinder height and the horizontal motion of the liquid is limited to small zones close to the bottom and the top surfaces of the liquid container. This is different for the fluid motion of test liquid II which is indicated by the streamline pattern in figure 13. The streamlines for the larger values of ψ^* are shifted upwards towards the free surface of the liquid and the streamline patterns close to the upper and lower liquid surfaces differ drastically.

The difference in the flow patterns for test liquid I and test liquid II is mainly caused by the difference in the fluid viscosities. Test liquid II has the lower viscosity and this causes the initial region to stretch; in this region the bubble velocity
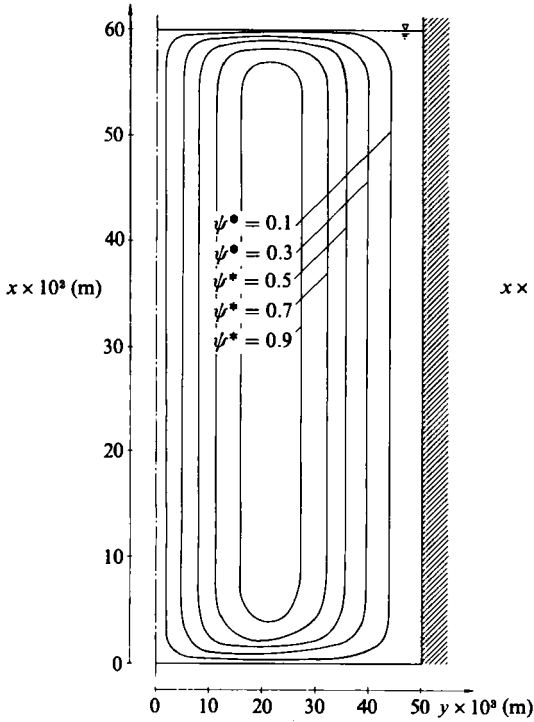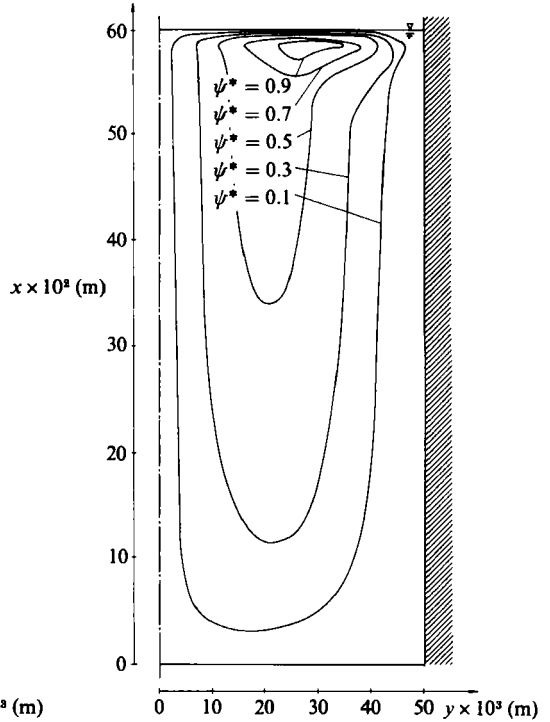
FIGURE 12. Streamlines for test liquid I with $f_b = 0.917$ Hz.

FIGURE 13. Streamlines for test liquid II with $f_b = 1.75$ Hz.
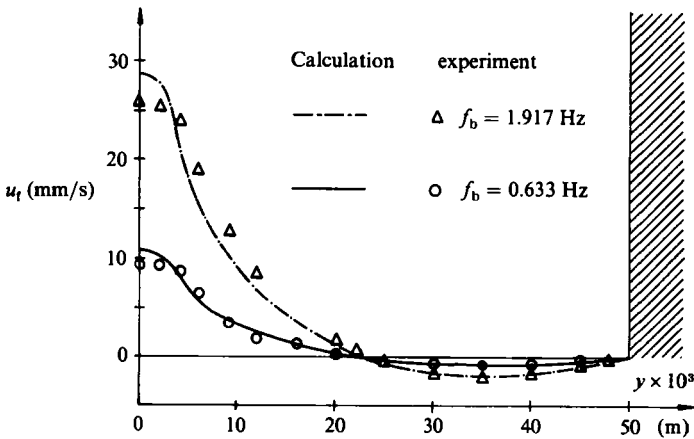

FIGURE 14. Theoretical and experimental liquid velocity across the test section (test liquid I).

increases with increasing distance from the bottom surface of the liquid container until the final rise velocity is reached. Because of the small viscosity of test liquid II, it 'takes longer' to transfer the bubble motion in the centre of the liquid container to the outer region of the fluid. For test liquid II low downward velocity close to the cylinder wall explains why experimental studies of this flow were sensitive to small differences between room and liquid temperatures; the difference in temperature gave rise to an upward flow, driven by free convection, and this interfered with the weak downward flow of the bubble-driven liquid motion close to the cylinder wall.

4.3.2. *Analytical solution of the fluid velocity for the 'developed' region*

It has been shown in figure 12 and figure 13, that the streamlines of the liquid flow are, over most parts of the test rig, parallel to the axis of the test section (at least for test liquid I).

Approximating the distribution of the volume concentration by step function:

$$\alpha = \begin{cases} \alpha_0 & (y < \frac{1}{2}d_e), \\ 0 & (y \geqslant \frac{1}{2}d_e), \end{cases} \tag{4.14}$$

permits the momentum equation for the liquid flow to be solved analytically for this 'developed' region. There the liquid velocity can be analytically derived by integrating the x-momentum equation to yield:

$$u_f(y) = \frac{g\,\Delta\rho\,\alpha_0\,d_e^2}{8\mu_f\,D^4}\left(D^2 - \frac{d_e^2}{2}\right)(D^2 - 4y^2)$$

$$- \frac{g\,\Delta\rho\,\alpha_0}{\mu_f}\begin{cases} \dfrac{d_e^2}{8}\ln\dfrac{D}{d_e} + \dfrac{1}{4}\left(\dfrac{d_e^2}{4} - y^2\right) & (y < \frac{1}{2}d_e), \\[2ex] \dfrac{d_e^2}{8}\ln\dfrac{D}{2y} & (y \geqslant \frac{1}{2}d_e). \end{cases} \tag{4.15}$$

In this equation the following quantities are employed:

u_f, fluid velocity,
g, gravity,
$\Delta\rho$, density difference,
D, diameter of the cylinder,
d_e, volume equivalent diameter of the bubble,
μ_f, dynamic viscosity of fluid.

As this equation shows, the drag coefficient expressing the fluid–bubble interaction does not explicitly appear in the equation for the fluid velocity. However, it enters the relationship implicitly since α_0 is dependent on the bubble velocity and therefore also on the drag coefficient of the bubbles. Using equations (4.12)–(4.15) permits the liquid velocity distribution in a cross-section of the cylindrical test section to be computed. Examples of computations are given in figure 14 for test liquid I and for two bubble frequencies. The figure also shows the corresponding experimental results and it can readily be seen that good agreement exists between the numerical and experimental data. Figure 15 shows that similar agreement is obtained for test liquid II over most of the cross-section of the cylindrical liquid container.

Considering the liquid motion, it can be readily deduced from (4.15) that for $d_e \ll D$, similar velocity distributions are obtained and can be analytically described as:

$$u_f^* = u_f(y)\bigg/\frac{g\,\Delta\rho\,\alpha_0\,d_e^2}{8\mu_f} \approx 1 - 4\left(\frac{y}{D}\right)^2 + \ln\frac{2y}{D}. \tag{4.16}$$

The change from the upward motion in the centre part of the test section and the downward motion in the outer part occurs at a location given as:

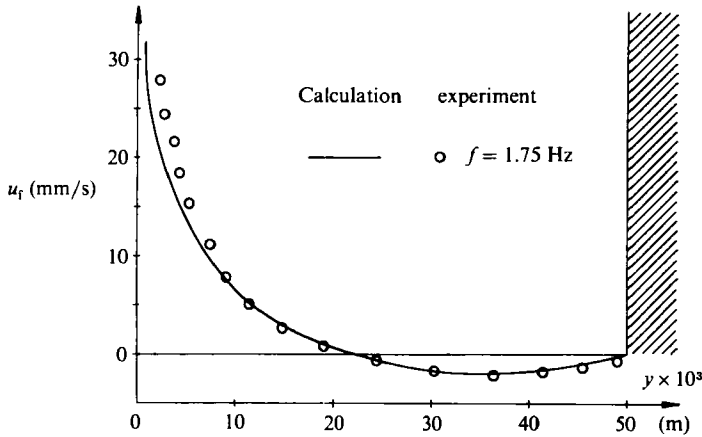$$y_0^* = \frac{y_0}{D} \approx 0.226. \tag{4.17}$$

FIGURE 15. Theoretical and experimental liquid velocity across the test section (test liquid II).

The resultant analytical expression for the liquid motion also shows the experimentally obtained linear dependence of the liquid flow rate of the upward or downward motion on the bubble frequency. The flow rate can be computed to be:

$$Q = 2\pi \int_{y_0}^{\frac{1}{2}D} u_f\, y\, \mathrm{d}y = \frac{g.D^2\Delta\rho\, d^3}{12 u_b \mu_f} \cdot f_b \cdot \underbrace{\left[2\pi \int_{y_0^*}^{\frac{1}{2}} u_f^*\, y^*\, \mathrm{d}y^* \right]}_{Q^*}. \qquad (4.18)$$

The above considerations were given for a top-hat distribution of gas volume concentration α_b as indicated in (4.14). It is worth noting that incorporation of the exact distribution, computed from the known bubble shape, the bubble rise velocity, and the bubble frequency, complicates the derivations but yields only small differences in the above results. This is due to the small region over which the gas volume concentration α_b differs from zero:

$$\frac{d_e}{D} < 0.07.$$

4.4. *Parameters influencing bubble-driven liquid flows*

Sections 3.2–4.3 show how the present treatment of bubble-driven liquid flow resulted in a generally applicable computer program in which all parameters influencing the flow can be freely varied. Applying this program to the liquid motion of test liquids I and II showed that quite different streamline patterns can result although both fluid motions are driven by bubbles rising along the centreline of a cylindrical liquid container. As the gas volume concentration α, the liquid viscosity μ_f, the diameter of liquid cylinder D, and the liquid height H, change, the streamline pattern of the flow varies accordingly. There are other parameters that influence the streamline patterns but some of them are less influential and were therefore not included in the parameter study presented here; e.g. since the bubble diameter is in most test cases much smaller than the diameter of the liquid container, the influence of the bubble diameter is not an important parameter and can be neglected for most of the predictions presented below.

Changing the above mentioned parameters, α, μ_f, D and H, numerical predictions of flow patterns have been performed for the test cases in table 2. The normalized

Test case	$M_b(\times 10^{-9})$	μ_t	D	H	d_e	ρ_t/ρ_b
1	1.57	0.01	0.1	0.6	0.002	1000
2	7.85	0.01	0.1	0.6	0.002	1000
3	1.57	0.05	0.1	0.6	0.002	1000
4	1.57	0.01	0.5	0.6	0.002	1000
5	1.57	0.01	0.1	0.3	0.002	1000
6	1.57	0.01	0.1	1.2	0.002	1000

TABLE 2. Parameters for fluid flow predictions (all values are given in MKS-units); $M_b \,\hat{=}\,$ gas mass flow rate.
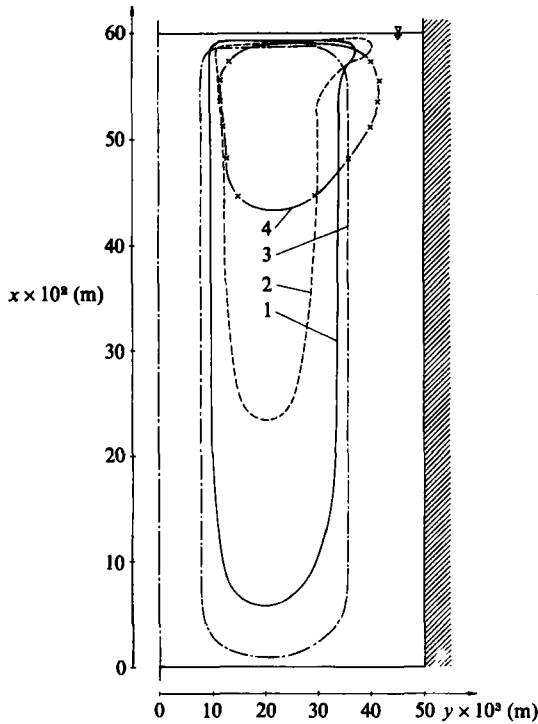
FIGURE 16. Streamlines for test case 1–4.

streamlines $\psi^* = 0.5$ are shown in figure 16 for the test cases 1–4. It can be seen from this figure, that with increasing gas mass flow rate, e.g. with increasing frequency of the introduced bubbles, the distance over which bubble acceleration occurs increases resulting in a ($\psi^* = 0.5$)-line which is moved upwards. This is indicated by comparing the streamlines for test case 1 and 2.

Increasing the viscosity of the test liquid changes the ($\psi^* = 0.5$)-line downwards. This is readily seen by comparing the streamline for test case 1 and the streamline for test case 3. Changing the ratio of the cylinder diameter to the liquid height from 6 to 1.2 as in test case 1 and 4, results in drastically different streamline pattern. The ($\psi^* = 0.5$)-line for case 4 is shifted upwards very close to the liquid surface.

In figure 17 the centreline velocities for the test cases 1–4 are given. This figure
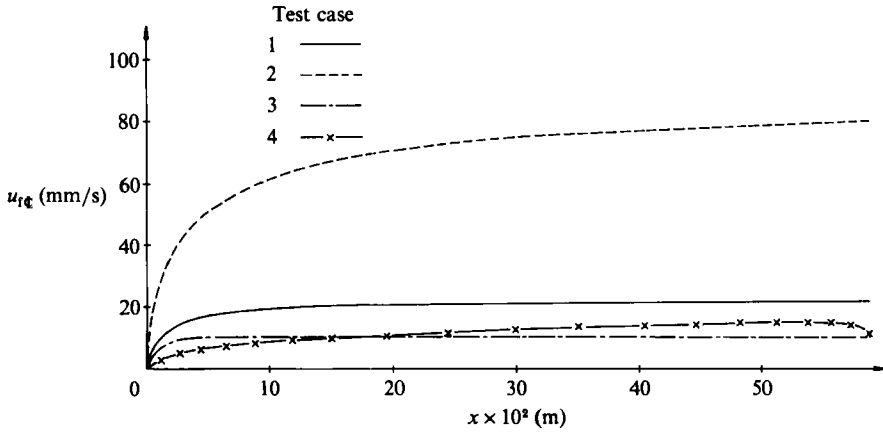
FIGURE 17. Centreline liquid velocity for test case 1–4.
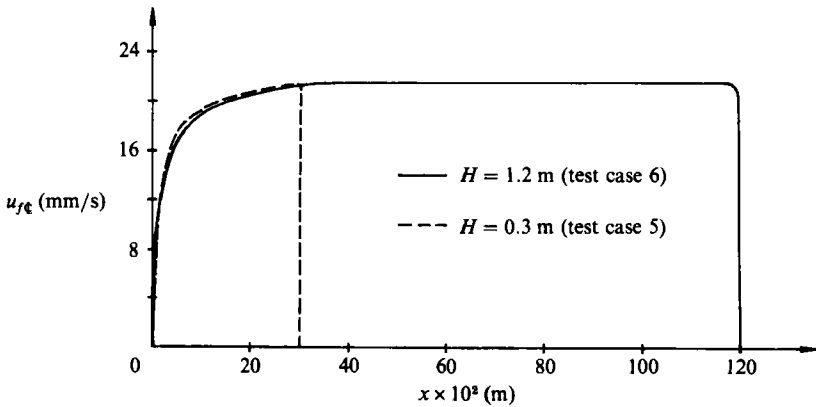

FIGURE 18. Centreline liquid velocity for different liquid heights in the cylinder.

indicates the different development length for the bubble velocity due to the different parameters of the bubble-driven liquid flow. It is clearly shown that the increase in the mass of the gas flow, causes an increase in liquid velocity, see test case 1 and 2 in figure 17. An increase in fluid viscosity causes a reduction in the rise velocity along the centreline of the cylindrical test section. Line 4 shows the different liquid velocity along the axis for a reduced ratio of H to D.

Test cases 5 and 6 have been performed for different heights of the liquid column. Figure 18 shows that the liquid centre velocity is hardly influenced by the liquid height. The bubbles can reach their maximum velocity if the liquid height is larger than 0.30 m. A decrease below this value would interfere with the bubble acceleration up to its terminal velocity and result in a changed streamline pattern.

4.5. Influence of 'bubble interface stiffening' on fluid motion

It is well known, and well documented, that the dynamics of rising bubbles is strongly influenced by the impurity content of the interface layer between the gas inside the bubble and the surrounding liquid. This dependence was also found in our experimental investigations and it is documented in §3.4 that the bubble velocity decreases with increasing distance from the bubble-generating nozzle after a velocity

maximum has been passed. For test liquid II, the bubbles did not reach the expected terminal velocity after the acceleration phase following bubble formation. Measurements for different water heights showed that the velocity decrease with height was not caused by the decrease of hydrostatic pressure experienced by the rising bubbles. Considerations of all the data for test liquid II indicated that the continuous bubble velocity decrease after the maximum velocity was caused by the extended exposure of the bubble interface layer to the impurities contained in the liquid. As figure 10 shows, the bubble velocity decreased with the length of time the fluid had been exposed to contamination through the surroundings. The increased concentration of impurities in the test liquid increased the speed of their settling in the bubble interface, and this in turn yielded an increased rate of velocity decrease with height.

Treating the bubble interface stiffening and its corresponding influence on the fluid motion theoretically, requires the reduction of the bubble surface mobility to be treated as a continuous modification of the drag coefficient of the rising bubble. To compute the drag coefficient variations due to bubble interface stiffening, Sadhal & Johnson (1983) provided an analytical treatment of the problem. They assumed that the impurities in the interface gather at the rear of the bubble and defined their so-called stiff-angle. This stiff-angle is a function of the amount of surface contamination present in the entire interface.

According to the analytical treatment of Sadhal & Johnson (1983), the drag coefficient can be expressed as a function of the stiff-angle ϕ ($C_D^* = C_D$ (bubble with impurities)$/C_D$ (clean bubble)):

$$C_D^* = \frac{1}{4\pi} (2\phi + \sin\phi - \sin 2\phi - \tfrac{1}{3}\sin 3\phi) + 1. \tag{4.19}$$

The stiff-angle is calculated by the following formula:

$$S(\phi) = A \cdot [2\phi - 4\phi \cos\phi - \sin 2\phi + 4\sin\phi], \tag{4.20}$$

in which the proportionality constant A will be a function of the liquid and gas properties and $S(\phi)$ expresses the amount of impurity in the bubble interface with the following limiting values:

$$S(0) = 0, \quad S(\pi) = 6\pi A.$$

With the assumption that S is proportional to the travelling distance of the bubble, the drag coefficient can be given as a function of the distance the bubble moved through the liquid. This results in the drag coefficient variation shown in figure 19. As the proportionality constant between the amount of impurity and the travelling distance of the bubble is not known in the present treatment, the x-distance in figure 19 has been normalized in such a way, that the drag coefficient reaches its maximum value $C_{D*} = 1.5$ at $x^* = 1$. The measurements showed that the amount of surface contamination is also a function of time the test liquid had been in the cylinder (see figure 10). For the present computations, this effect has been modelled by introducing a factor $f(t)$ in equation (4.20), which varies between 0 and 1. The normalized travelling distance x^* can now be written as

$$x^* = \frac{1}{6\pi f(t)} (2\phi - 4\phi \cos\phi - \sin 2\phi + 4\sin\phi), \tag{4.21}$$

that is
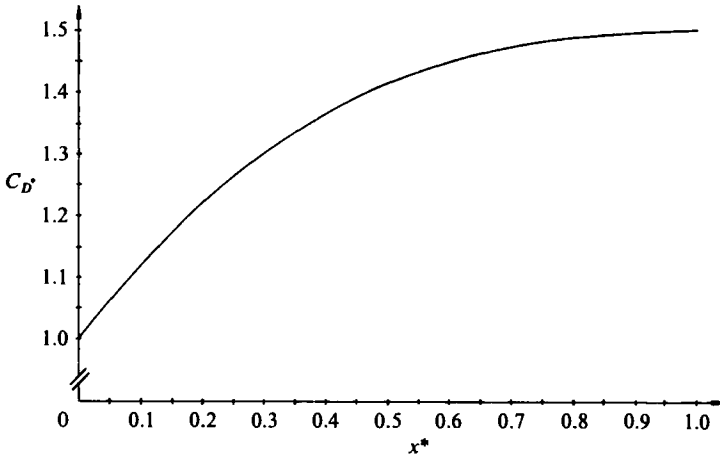$$x^*(0) = 0, \quad x^*(\pi) = \frac{1}{f(t)}.$$

FIGURE 19. Drag coefficient for bubbles with increasing impurity content in the interface layer.
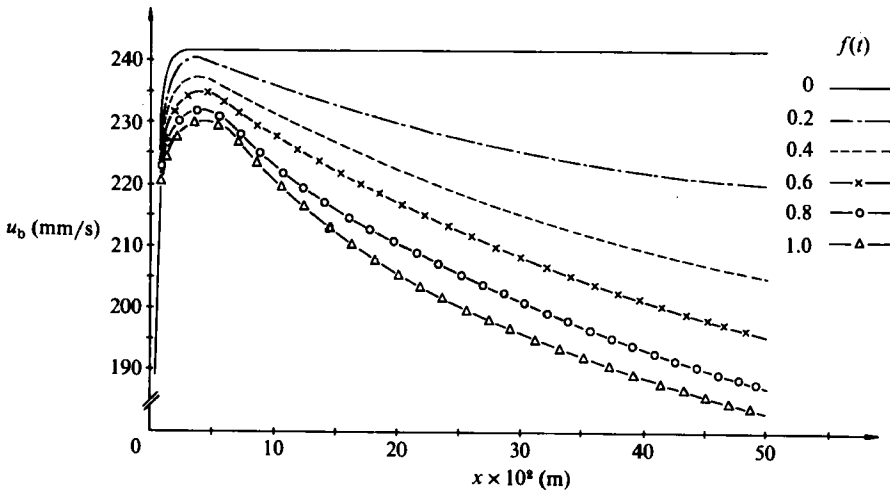
FIGURE 20. Bubble velocity with travelling distance.

The drag coefficient as a function of the travelling distance is obtained with the help of (4.19) and (4.21). Using this modified drag coefficient, the bubble rise velocity in a stagnant fluid is obtained as a function of the travelling distance of the bubble and the time the liquid rested in the cylinder. Figure 20 presents computations of the bubble rise velocity as a function of travelling distance for various values of $f(t)$. It is shown that the bubble velocity variations computed are very similar to the experimental data given in figure 10. The good agreement between the computed and the experimental maximum velocities and the agreement of shapes of the velocity variation curves justify the assumption that the decrease in bubble velocity with height is caused by the impurities settling in the bubble interface. Due to lack of information, more detailed and more quantitative results cannot be obtained. Too little is known about the impurity contents relevant to bubble interface stiffening; theoretical treatments have to handle the phenomena in the global way presented above. More quantitative experimental studies are needed to get more detailed information on the mechanisms by which impurities enter the bubble surface and cause the stiffening of the bubble interface.

5. Conclusions and final remarks

We have considered the liquid flow induced by rising bubbles inside a circular cylinder with a vertical axis. A brief summary of the existing knowledge shows that detailed information on the flow inside and around bubbles is not available. Laser-Doppler anemometry is employed to provide the missing information by measuring the rising velocity of the bubbles as well as the entire velocity field induced in the liquid. Predictions are made, which allow the calculation of the bubble velocity and the liquid velocity field by prescribing only the gas volume flow rate and the bubble diameter.

To carry out the bubble velocity measurements and also to obtain measurements of the liquid velocity in the fluid, an extended laser-Doppler anemometer is employed together with a fast data-acquisition system to map out the entire flow field around bubbles. Two bubbles are studied in detail and are characterized by their Reynolds number and Eötvös number. Carrying out bubble velocity measurements for various bubble frequencies, permits the terminal velocity of a single bubble to be obtained by extrapolation of the rising velocity down to the values for zero bubble frequency. It is shown that the measured terminal velocity is higher than that obtained for solid particles and lies very close to the terminal velocity of rising liquid particles. Information for comparison on the terminal velocity is taken from the literature. The LDA-measurements show that there is no flow separation at the back of the bubble even for the investigated bubble with $Re = 64$. This indicates that the bubble interface is 'in motion' due to the flow field of the air inside the bubble.

However, 'stiffening' of the bubble interface can occur if impurities are present in the liquid. These will cause the bubble rise velocity to decrease with the distance of the bubble from the nozzle.

A computer program has been developed to predict the velocity of rising bubbles as well as the flow field they induced in the surrounding liquid. The prediction procedure is based on the two-phase flow equations and only employs information on the gas volume flow rate and the bubble diameter to yield the information on the flow fields of rising bubbles *and* the fluid. It is shown that the numerical predictions agree well with experiments. For the region where the streamlines of the liquid motion can be considered parallel to the trajectory of the rising bubbles the partial differential equation for liquid motion can be solved analytically. The resultant analytical expression is given and it is shown that it describes the liquid flow field in those regions very well.

The experimentally observed bubble stiffening is dealt with in the theoretical derivations and it is shown that the experimentally observed variation of the bubble velocity with the height above the nozzle can be theoretically explained. There was good agreement between measurements and predictions.

The paper stresses that the combined use of computer programs and the extended laser-Doppler anemometer for studies of particulate two-phase flows permits the present physical understanding of simple two-phase flows to be advanced. Extensions of the work to more complex two-phase flows are suggested.

REFERENCES

AUTON, T. J. 1984 The dynamics of bubbles, drops and particles in liquids. Ph.D. thesis, University of Cambridge.

BRANKOVIC, A., BÖRNER, T. & MARTIN, W. W. 1984 The measurement of mass transfer coefficients of bubbles rising in liquids using laser-Doppler anemometry. In *Laser Anemometry in Fluid Mechanics* (ed. D. F. G. Durao). Lisbon: Ladoan.

BRAUER, H. 1982 Movement of single particles in various flow fields. In *Advances in Transport Processes* (ed. A. S. Mujumdar & R. A. Masbelkar), p. 352. New Delhi: Wiley Eastern.

CLIFT, R., GRACE, J. R. & WEBER, M. E. 1978 *Bubbles, Drops and Particles*. Academic.

DURST, F. & ZARÉ, M. 1975 Laser-Doppler measurements in two-phase flows. *Proc. LDA-Symposium, Copenhagen*, p. 403.

DURST, F., MELLING, A. & WHITELAW, J. H. 1976 *Principles and Practice of Laser-Doppler Anemometry*. Academic.

DURST, F., SCHÖNUNG, B. & SIMONS, M. 1981 Steady Ellipsoidal Vortex Rings with Finite Cores. *Z. angew. Math. Phys.* 32, 156.

DURST, F., TAYLOR, A. M. K. P. & WHITELAW, J. H. 1984a Experimental and numerical investigation of confined, laminar, bubble-driven liquid flow. *Intl J. Multiphase Flow* 10, 557.

DURST, F., MILOJEVIC, D. & SCHÖNUNG, B. 1984b Eulerian and Lagrangian predictions of particulate two-phase flows: a numerical study. *Appl. Math. Modelling* 8, 101.

GOLDSTEIN, S. 1929 The steady flow of viscous fluid past a fixed spherical obstacle at small Reynolds numbers. *Proc. R. Soc. Lond.* A 123, 225.

GOVIER, G. W. & AZIZ, K. 1972 *The Flow of Complex Mixtures in Pipes*. Van Nostrand Reinhold.

HADAMARD, M. J. 1911 *C. R. hebd. Séanc. Acad. Sci.* 152, 1735.

HARPER, J. F. 1972 The motion of bubbles and drops through liquids. *Adv. Appl. Mech.* 12, 59.

LEVICH, V. G. 1962 *Physiochemical Hydrodynamics*. Prentice-Hall.

MARTIN, W. W., ADBELMESSIH, A. H., LISKA, J. J. & DURST, F. 1981 Characteristics of Laser-Doppler signals from bubbles. *Intl J. Multiphase Flow* 7, 439.

MARTIN, W. W. & CHANDLER, G. M. 1982 The local measurement of size and velocity of bubbles rising in grids. *Appl. Sci. Res.* 38, 239.

MIKSIS, M. J., VANDEN-BROECK, J. M. & KELLER, J. B. 1982 Rising bubbles. *J. Fluid Mech.* 123, 31.

OSEEN, C. W. 1927 *Neuere Methoden und Ergebnisse in der Hydromechanik*. Leipzig: Akademische Verlagsges.

PAN, F. Y. & ACRIVOS, A. 1968 Shape of a drop or bubble at low Reynolds number. *I & EC Fundamentals*, 7, 227.

RYBCZYNSKI, W. 1911 Über die fortschreitende Bewegung einer flüssigen Kugel. *Bull. Acad. Sci. Cracow* A 40.

SADHAL, S. S. & JOHNSON, R. E. 1983 Stokes flow past bubbles and drops partially coated with thin films. *J. Fluid Mech.* 126, 237.

SCHÖNUNG, B. 1983 Numerische Simulation teilchenbeladener vertikaler Rohrströmungen. Ph.D. thesis, Universität Karlsruhe.

STOKES, G. G. 1891 On the effect of the internal friction of fluids on the motion of pendulum. *Math. Phys. Papers* 3, 55.